J. Indian Chem. Soc.,
Vol. 96, January 2019, pp. 187-197

Enhanced magnetic and catalytic properties of copper substituted barium M-hexagonal ferrites synthesized from chemical co-precipitation method

T. L. Ajeesha, Ashwini Anantharaman and Mary George*

Department of Chemistry, Stella Maris College, Chennai-600 086, India

E-mail: maryge@gmail.com

Manuscript received online 30 August 2018, accepted 10 October 2018

Discharge of organic chemicals in to the water bodies leads problems to both human and aquatic life. Barium hexaferrite is an effective catalyst in the rapid degradation of methylene blue dye. In this regard, the present study was focused on synthesis of copper substituted barium photocatalyst by co-precipitation method and the as-synthesized materials were calcined at 650°C for 8 h to form the corresponding ferrites. The obtained ferrites were characterized by UV-DRS, Fourier Transform Infrared (FT-IR), Powder X-ray Diffraction (PXRD), Transmission Electron Microscope (TEM), Vibrating Sample Magnetometer (VSM), Brunauer-Emmett-Teller (BET) techniques to study their structural, optical and magnetic properties respectively. The results indicate the substitution of copper in barium ferrite nanomaterials strongly influences the crystal structure and magnetic properties of the synthesized nanomaterial.

Keywords: Spinel, co-precipitation, hexagonal ferrites, photocatalytic degradation.

Introduction

Water sources are prominently affected by pollutants and toxic contaminants. The presence of industrial waste water dyes in environment create problems due to its high toxicity. Presence of low concentrations dyes in water reduces light penetration to the water surface, preventing photosynthesis of the aquatic plants. Synthetic organic dyes are mutagenic, teratogenic and carcinogenic. These organic pollutants are toxic to human beings, microorganism and the aquatic life, therefore their removal from polluted water is essential for environmental protection. Dangerous synthetic dye organic pollutants are easily degraded by the photocatalyst due to their synthetic origin and aromatic nature. Iron oxide photocatalyst holds catalytic properties for reaction such as decomposition of hydrogen peroxide, alcohols, discoloration of synthetic dyes and selective oxidation of carbon monoxide[1–3]. Presently, the attempts in introducing stable and efficient light induced photocatalysts are of large scale for its superior proficiency in utilizing the solar energy. The photocatalyst with semiconductor properties are widely used for degradation of organic contaminants for the remediation of hazardous wastes and polluted ground water and the control of toxic air pollutants. Barium ferrite is well-known as a permanent magnet, because of its high Curie temperature, high coercivity, large crystalline anisotropy, and high magnetization. Hexagonal barium ferrites are used in recording materials because of its high packing capacity. The magnetic properties of hexagonal spinel ferrites are controlled by regulating the particle size, morphology, size distribution and microstructure. Barium hexa ferrite is a low band energy ferrite material with large magneto crystalline anisotropy, relatively large magnetization as well as chemical and corrosion stability. Borse *et al*. reported the synthesis of barium ferrite and their optical and photocatalytic applications. Investigation of barium ferrite nanoparticles by co-precipitation method was reported by Liu *et al*. The introduction of copper metal-ion spin dynamics and also causes the visible light absorptivity of the material, packing density and storage capacity increases with increase in surface area[5–9]. Several methods like the mechanical milling, auto-combustion, hydrothermal, ceramic, sol-gel, microwave conventional method and co-precipitation techniques are available by which the spinel ferrite nanomaterials are prepared. The aim of this work was to investigate the structural, optical, magnetic and catalytic properties of copper substituted barium M-hexagonal ferrites via the chemical co-precipitation method. The as-synthesized nano photocatalyst was used in the degradation study of

Methylene blue (MB) organic dye used widely in the textile industry.

Materials and methods:

The AR grade inorganic chemicals were used without purification for the synthesis of copper substituted barium ferrite nanomaterials. The stoichiometric amount of $Ba_{1-x}Cu_xFe_2O_4$ (x = 0.0, 0.2, 0.4, 0.6, 0.8, 1) spinel ferrites were prepared by chemical co-precipitation technique. Barium nitrate (Nice chemicals) ($Ba(NO_3)_2$), copper nitrate (Fisher's scientific) ($Cu(NO_3)_2$) and ferric nitrate (Merck) ($Fe(NO_3)_3$) were dissolved in 50 mL deionized water separately and stirred well. The dissolved solution was kept for stirring and mineralizer (2 *M* NaOH) was added to maintain the pH at 13. The solutions were heated at 80°C for 3 h until a brown precipitate was obtained. The obtained brown precipitate was washed with deionized water to make it free from nitrate ions; the obtained mixture was annealed at 75°C for 24 h in a hot air oven. After drying, the resulting by-products were grounded to fine powdered and then calcinated at 650°C in a muffle furnace for 8 h to obtain $Ba_{1-x}Cu_xFe_2O_4$ nanomaterials.

Antibacterial studies:

The antibacterial activities of the as synthesized $Ba_{1-x}Cu_xFe_2O_4$ nanomaterials were studied using the measurable well diffusion assay. All glassware, media and reagents used were sterilized in a autoclave at 121°C pressure chamber at 100°C for 15 min. Muller Hinton agar was used as a test medium for antibacterial susceptibility testing. Gram-positive (*Staphylococcus aureus*, *Bacillus subtilis*, *Micrococcus luteus*), Gram-negative (*Enterobacter aerogenes*, *Escherichia coli*) were used as model test strains. Microbes were marbled on the surface by means of a sterile cotton swab. 5–7 wells (10 mm diameter) were made by using a sterile cork borer. The 2 different concentrations (25 mg and 50 mg) of $Ba_{1-x}Cu_xFe_2O_4$ nanomaterials were loaded in the wells. The plates were incubated at 27°C for 24 h and they were examined for the efficiency of $Ba_{1-x}Cu_xFe_2O_4$ nanomaterials by measuring the zone of inhibition. After 24 h of incubation, bacterial suspension was diluted with sterile physiological solution for the well diffusion tests.

Physical characterization:

The crystallite size and phase structure of $Ba_{1-x}Cu_xFe_2O_4$ Power XRD is used. Brucker AXS D8 Advanced with Cuα irradiation (wavelength λ = 0.15418 nm). The diffracted X-ray beam was collected by scanning Si (Li) PSD detector, with the temperature range of –170°C to + 450°C. The surface morphology was determined by JEOL/JEM 2100, source LaB6 with 200 K and the camera length is 80–200 mm. The magnetic properties of the as-synthesized nano power were measured by using Lakeshore VSM 7407 with magnetic field 2.5 T at room temperature (303 K) in a maximum applied field of 15000 Gauss. From the obtained hysteresis loops the saturation magnetization (M_s) and corecivity (H_c) were obtained. The pore size distribution, surface volume and surface area are given by BJH (Barrett-Joyner-Halenda) and BET (Brunauer-Emmett-Teller) method using Quantachrome ® ASiQwinTM instrument. UV-Diffused Reflectance Spectra (DRS) is used to study the optical properties of the synthesized nano spinel ferrite, JASCO V-750 UV-Vis spectrophotometer. The photocatalytic activities were done using HEBER multilamp reactor and the degradation efficiency was studied by using JASCO V-750 UV-Vis spectrophotometer.

Photocatalytic activity of the copper substituted barium ferrite nanomaterials was calculated by measuring the photocatalytic degradation of Methylene blue ($C_{16}H_{18}ClN_3S$) in deionized water under the irradiation of UV-light (HEBER multi lamp photo reactor) using UV-Visible spectrophotometer (JASCO 750). 100 ppm of Methylene blue dye with 0.1 g of the as-synthesized nanophotocatalyst then transferred to the quartz tubes used for irradiation experiments. The tubes were exposed to the UV-lamp for 180 min at room temperature. The maximum absorption band for Methylene blue dye was found to be 665 nm. In order to study the photocatalytic activities of $Ba_{1-x}Cu_xFe_2O_4$, the mineralization of Methylene blue dye was done and its absorption was studied by UV-Visible (JASCO 750) spectrophotometer. The photocatalytic degradation was decreased 97 to 86 for BCFO-2 this may be due to decrease in the surface area.

Results and discussion

Powder X-ray diffraction studies:

The PXRD patterns for $Ba_{1-x}Cu_xFe_2O_4$ were recorded in the region of 2θ = 10–80°C with a stop scan of 3° to 135° on a diffractometry using Cu Kα radiation. The crystallite size was determined from the diffraction image of the strongest peak by using Scherrer formula $D = K\lambda/(\beta \cos\theta)$; K = Scherrer

constant (K = 0.9), t = average size of the crystallite, λ = wavelength of radiation (λ = 1.54056 nm), β = full width half maximum of the diffraction peak at θ and θ = diffraction angle corresponds to the peak position measured in radius. The average crystalline size was found to be 18–30 nm and the structure was found to be hexagonal with the space group R3m. JCPDS (78-0133) diffraction files were used to match the formed phases. The strong diffraction peaks of pure and substituted barium hexaferrite samples exhibit at (210) plane and the standard peaks at 2θ values corresponding to (100), (200), (212), (220), (320) planes respectively. XRD diffractogram shows a shift in the intensities on increasing Cu^{2+} concentration. The shift in peaks is confirmed by Bragg's law. It was found that as the Cu^{2+} concentration increases the particle size gradually decreases. The decrease in particle size, which is attributed to hardening and growth of smaller particles on the surface[14–16]. The lattice parameter (a) decreased with increase in Cu^{2+} substitution. This is due to the comparatively small ionic radius of Cu^{2+} (0.73 Å) comparing to Fe^{3+} (0.78 Å) ionic radius. This confirmed that the synthesized ferrite is nanocrystalline in nature. No extra peaks are found in the diffractograms indicating that the synthesized nanomaterials with high phase purity can be obtained by the co-precipitation method[17–19]. The lattice constant "a" was calculated from the following relationship:

$$1/d^2 = 4/3\ [(h^2 + hk + k^2)/a^2] + 1/c^2$$

where d is diffracting plane spacing and (h, k, l) miller indices of the diffracting plane and the lattice constant (a) values are given in Table 1. Cu^{2+} concentration increases with decrease in lattice constant (a). The XRD density (PXRD) was calculated by the formula:

$$dx = 8M/(Na^3) = (a_x)\ (g/cm^3)$$

where, M is sub-atomic weight of the sample and N is Avogadro's number and 'a' is the lattice parameter. The thickness (a_x) depends on the lattice parameter and sub-atomic weight of the sample. Dislocation density (δ)[20] is used to determine the dislocations in unit volume of the synthesized crystalline nanomaterials (Table 1).

$$\delta = 1/D^2$$

where D is the crystallite size of the synthesized nanomaterials, it is clearly seen that as the substitution concentration is increased the dislocation density increases indicating that the Cu^{2+} ions from microstrain in the lattice site.

Williamson-Hall method:

Stress and strain induced crystal distortion is given by elastic strain ($\varepsilon = \beta/2\cot\theta$) and the elastic constant values are given Table 1. Elastic strain of BCFO-2 is higher than BCFO-1 and BCFO-3, this is due to the substitution of Cu^{2+} in barium ferrite. Using Williamson-Hall method, the crystalline size of samples is known and the W-H plot is given by,

$$\beta \cos\theta = [k\lambda/D] + 4\varepsilon \sin\theta$$

Table 1. PXRD parameters for BCFO-1, BCFO-2, BCFO-3 nanomaterials

Compound name	Elastic strain $\varepsilon = \beta/2\cot\theta$ ($\times10^{-3}$)	W-H $\beta\cos\theta$	W-H $4\sin\theta$	Interplanar distance (d)	Lattice constant (Å)	X-Ray density (a_x) (g/cm^3)	Dislocation density (δ)
BCFO-1	0.00174	0.31914	0.0545	2.7680	8.1879	8.324	0.0016
BCFO-2	0.00309	0.35252	0.0610	2.6172	8.2411	8.401	0.0020
BCFO-3	0.00192	0.42043	0.0729	2.5277	8.1053	8.542	0.0023

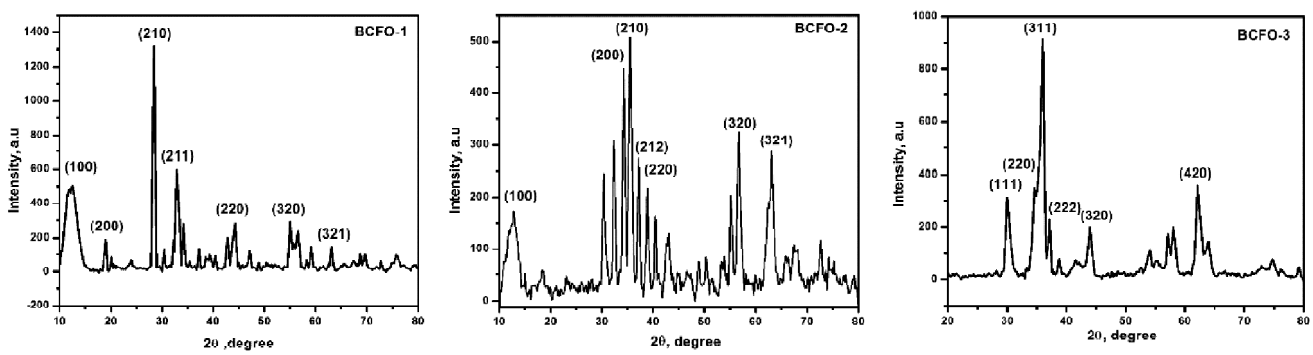

Fig. 1. PXRD pattern for BCFO-1, BCFO-2 and BCFO-3.

k is constant (0.9), λ is the wavelength of X-ray source (1.5409), *D* is the crystallite size, β be the full width half maximum of the specified diffracted peak and ε is elastic strain of the samples. Using the above relation the W-H plot is drawn in Fig. 1.1.

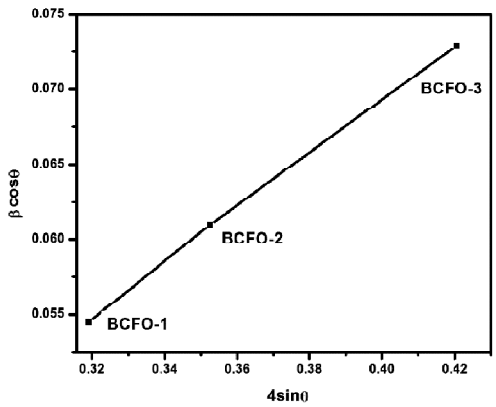

Fig. 1.1. W-H analysis plot for BCFO-1, BCFO-2 and BCFO-3.

Size-strain plot:

Williamson-Hall plot demonstrates that, due to microstrain the diffracting domains were isotropic. Size-strain parameters can be obtained from size-strain plot (SSP). This is advantageous for the less positioned data from reflections at the high angles. In this aspect it is assumed that the plot is illustrated by strain plot by a Gaussian function and the crystallite size by Lorentzian function. Hence we have,

$$(d\beta\cos\theta)^2 = K/D\,(d^2\beta\cos\theta) + (\varepsilon/2)^2$$

where *k* is constant (0.9), *D* is crystallite size and ε is elastic strain. The slope linearly fitted data and the root of the Y-intercept is given in Fig. 1.2 and Fig. 1.2a represents the Scherrer plot for the synthesized nanomaterials.

Fourier Transformer-Infra Red spectroscopic analysis:

From FTIR spectrum high and low frequency absorption bands corresponding to stretching vibrations are analyzed. The absorption peaks freely depend on the crystalline nature, morphology and chemical composition of the materials in order to determine the chemical bonding nature of pure and substituted barium ferrite compounds (Fig. 2) of annealed $Ba_{1-x}Cu_xFe_2O_4$ at 6500C shows two absorption bands below 600 cm^{-1}, a common feature of all spinel ferrites. The frequency band (γ1) lies in the 580–600 cm^{-1} and the low frequency band (γ2) in the range of 400–430 cm^{-1}. The difference in the band position is attributed to the vibration of td and oh sites in the spinel ferrites. The band at 421 and 586 cm^{-1} attributes to Ba-O and Fe-O stretching vibrations and 1630, 2010, 2600 cm^{-1} are caused by band strength of -OH groups. The vibrations of Fe-O is the frequency band range low frequency wavenumber is 472, 524 cm^{-1} for sintered samples, the FTIR band at 3406, 3455, 1637 cm^{-1} can be

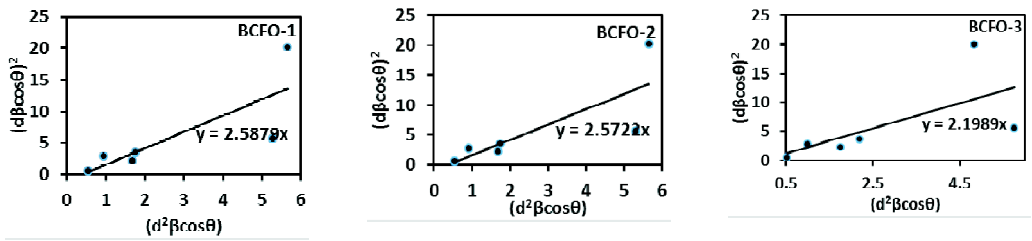

Fig. 1.2. Size-strain plots for BCFO-1, BCFO-2 and BCFO-3 nanomaterials.

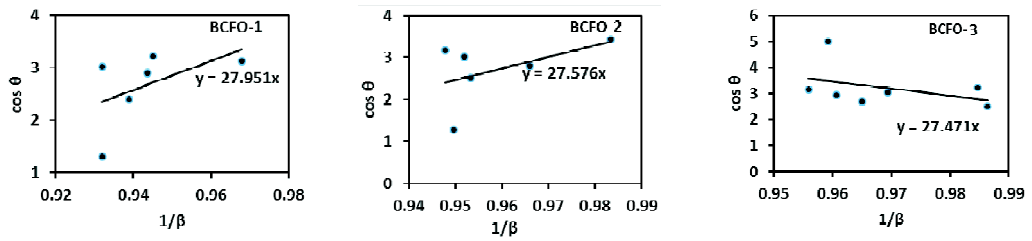

Fig. 1.2a. Scherrer plots for BCFO-1, BCFO-2 and BCFO-3 nanomaterials.

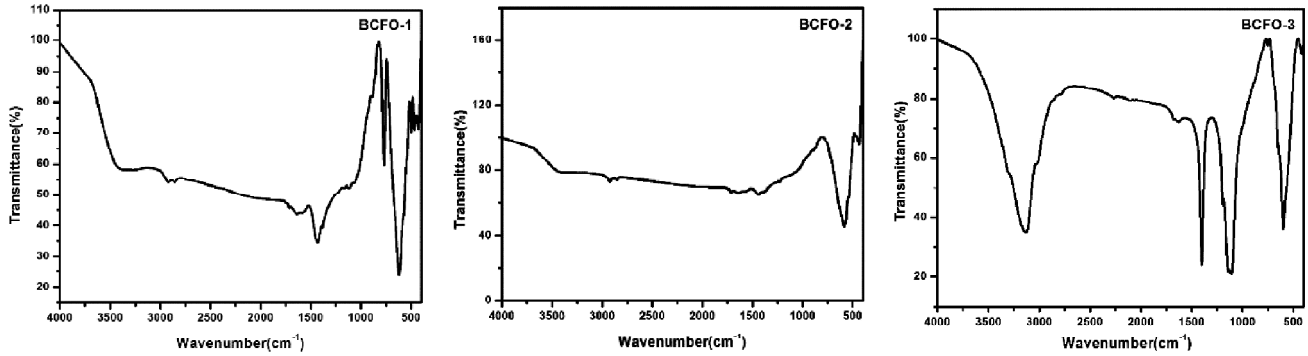

Fig. 2. FT-IR spectra for BCFO-1, BCFO-2 and BCFO-3 nanomaterials.

assigned to the vibration of -OH groups and the samples have some relation mean while the relative strength of peak has also changed this may be caused by -OH removes through sintering[1,21,22]. Table 2 provides information about the elastic and mechanical properties of the synthesized nanomaterials.

Morphological studies:

TEM (Jeol/JEM 2100 and magnification ranges from 2000 X–1500000 X) micrographs represent the surface morphology of the synthesized spinel nanomaterial. Fig. 3 shows the Transmission Electron Micrographs of different concentration of $Ba_{1-x}Cu_xFe_2O_4$. The micrograph depicts the degree of agglomeration of the nanomaterials due to its magnetic property and by the weak Van der Waals force. The surface morphology of the synthesized nanomaterials was of rod shape and found to be mesoporous in nature. Copper ferrite is considered to be a normal spinel and barium ferrite is an inverse spinel. Addition of Cu^{2+} in barium ferrite leads to change in cation distribution and thereby barium ferrite occupies the octahedral site which is more lateral and they experience a strong magnetic moment relative to the volume[22–24]. Bright crystalline diffraction ring spots in selected area electron diffraction pattern (SAED) indicate the spinel structure of $Ba_{1-x}Cu_xFe_2O_4$ oxide nanomaterials.

VSM:

The magnetic property of $Ba_{1-x}Cu_xFe_2O_4$ nanomaterials was depicted by VSM (Lakeshore VSM 7407 with magnetic field 2.5 T at room temperature (303 K)). The hysteresis loop shows the synthesized nanomaterials BCFO-1 and BCFO-2 is a hard ferrite; BCFO-3 is soft ferrite. The high coercivity value for BCFO-1and BCFO-2 nanomaterials experience the magnetic anisotropic effect on the surface and existence of dominant pinning sites at the interfaces of the spinel ferrite. The coercivity (H_c) was found to be 6056.6 G, 3378.3 G and 503.69 G for BCFO-1, BCFO-2 and BCFO-3 respectively. The magnetic moment (μB) was calculated by the relation

$$\mu B = M \times M_s/5855$$

where, M is the molar mass and M_s is the saturation magnetization. Magnetic moment (μB) values are given in Table 3. As the addition of Cu^{2+} divalent cation increases, the saturation magnetization is also increased from BCFO-1 to BCFO-3 and from the ratio (M_r/M_s), the squareness ratio (SQR) is obtained and the squareness ratio for BCFO-1 to BCFO-3 is given in Table 3. Fig. 4a showed the variation of magnetic anisotropy field with Ba-Cu concentration for all samples. It is clear that Ha decreases with increasing the concentration $X = 0.2$[15,25]. The SQR for BCFO-1 is higher because of its high coercivity and magneto anisotropy effect leading the

Table 2. Parameters for elastic and mechanical properties for BCFO-1, BCFO-2, BCFO-3 nanomaterials

Compound name	$\gamma_{\alpha\beta}$	Debye temperature (O_D)	Force constant (Newton) T_d	Force constant (Newton) O_h	Stiffness constant (N/m)	Elastic constant (p_a)	Bulk modulus (p_a)	Rigidity modulus (p_a)
BCFO-1	511.4	1,478	0.0423	0.040	0.0417	0.0449	0.0124	0.0162
BCFO-2	503	1,142	0.0418	0.038	0.0408	0.0329	0.0119	0.0314
BCFO-3	511	1,484	0.0433	0.031	0.0371	0.0303	0.0114	0.0287

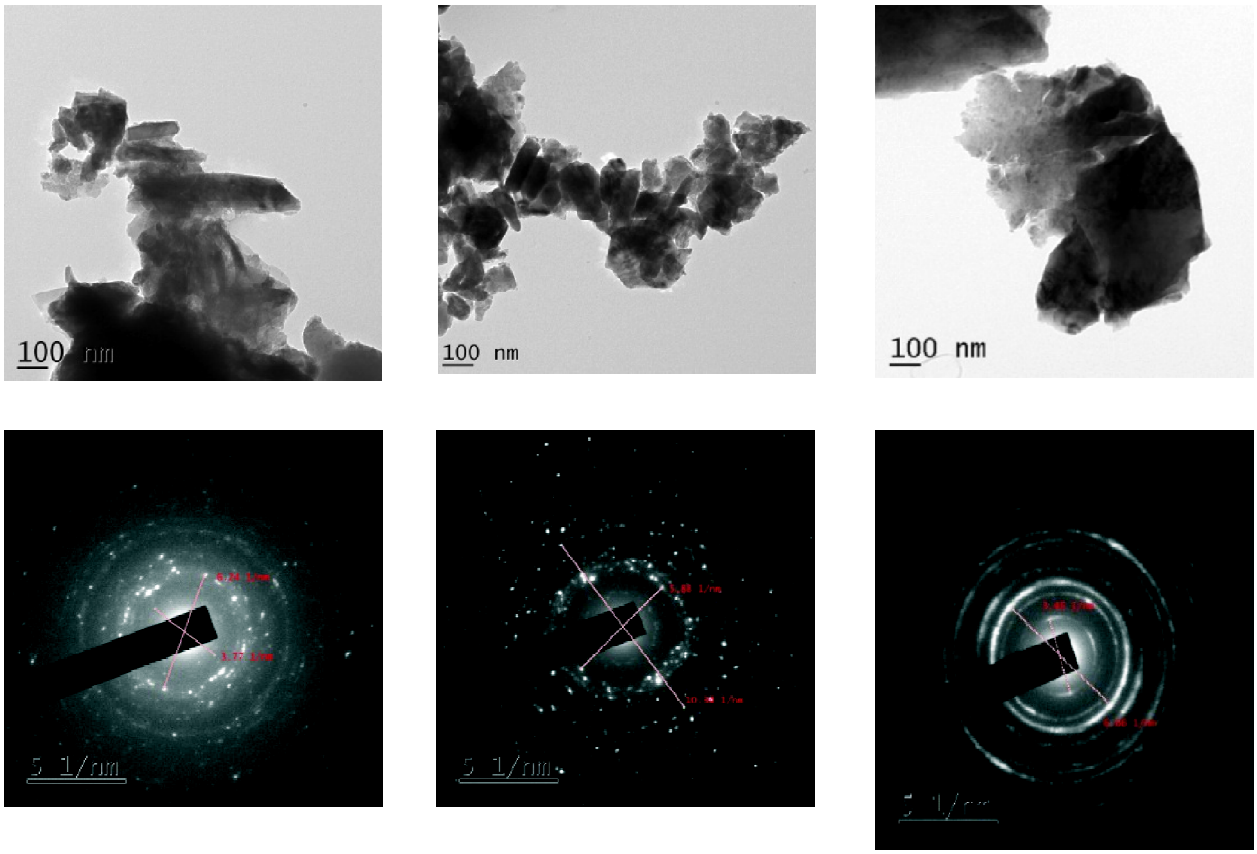

Fig. 3. TEM micrographs for BCFO-1, BCFO-2 and BCFO-3 nanomaterials.

Table 3. Magnetic parameters of BCFO-1, BCFO-2, BCFO-3 nanomaterials

Compound name	Coercivity (H_{ci}) (G)	Magnetization (M_s) (emu)	Retentivity (M_r) (emu)	Squareness ratio (M_r/M_s)	Magnetic moment (μB)T or kg s^{-2} A^{-1}
BCFO-1	6056.6	0.32696	0.18775	0.57	0.0210
BCFO-2	3378.3	0.76042	0.42195	0.55	0.0489
BCFO-3	503.69	1.2431	0.43547	0.35	0.0098

compound to be a hard ferrite. Large (squareness ratio) SQR values are preferred in many magnetic storage applications such as magnetic recording media of high density. The more percentage of copper substituted barium ferrite materials can exhibit a higher magnetization and magnetic storage capacity. And in case of $Ba_{1-x}Cu_xFe_2O_4$ spinel nanomaterials the particle size was found to be smaller to have less surface area and high force of demagnetization effect.

Nitrogen adsorption/desorption studies:

The BET analysis was determined from Emmett-Teller adsorption-desorption isotherm at 77 K for $Ba_{1-x}Cu_xFe_2O_4$ nanomaterials, it shows the adsorption branch does not take path of desorption branch, results in type II isotherm with adsorbent material consisting of agglomerated uniform rods. On captivating the N_2, the samples are enriched by increasing the relative pressure, at the same time desorption branch reflects type II isotherm that is generally associated with mesoporous material formation in the diameter range of 18–30 nm. It is substantial to note that the surface area decreases as the particle size increases[21]. This decrease in surface area is significant to the photocatalytic activity of the as-syn-

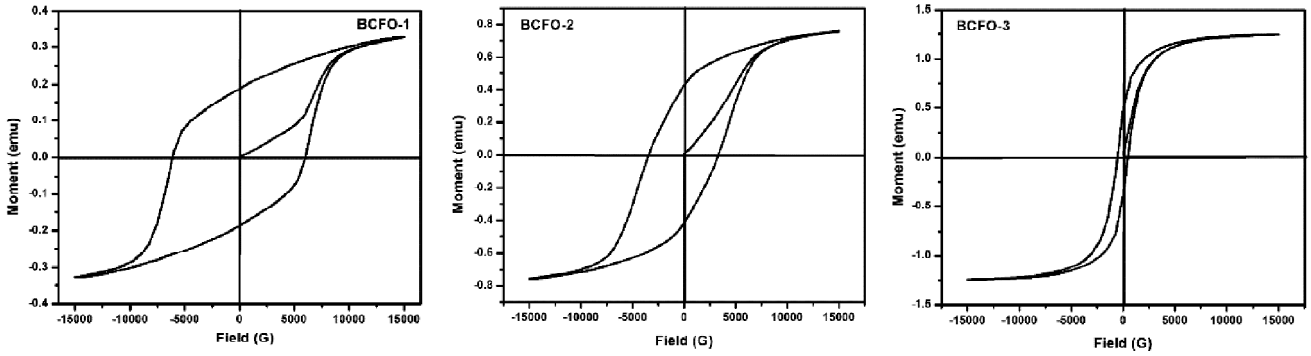

Fig. 4. Hysteresis loops for BCFO-1, BCFO-2 and BCFO-3 nanomaterials.

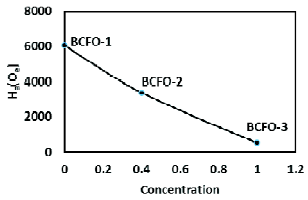

Fig. 4a. Anisotropy field of BCFO-1, BCFO-2 and bCFO-3 nanomaterials.

thesized nanomaterial. The pore distribution curve shows the absence of narrow size pore distribution. The pore diameter of BCFO-2 is high when compared to BCFO-1 and BCFO-3, this is due to the addition of copper in barium ferrite and this leads the compound to have a high pore width (Table 4).

Optical studies:

The absorption spectra of the as-synthesized $Ba_{1-x}Cu_xFe_2O_4$ spinel nanomaterials are shown in Fig. 7. The absorption bands for the synthesized nanomaterials are shown in Table 5. The difference in absorbance edge is due to the incidence of point defect and photon-electron interaction. The band gap energy is determined by direct transition equation, $(\alpha h\nu) = A\,(h\nu - E_g)n$, where α, v, E_g, h, A are proportionality constant, light frequency, band gap, Planck constant and absorption coefficient[20]. The band gap decreases as the copper concentration increases shown in Fig. 6a. The band gap energies are found to be decreased from BCFO-1 to BCFO-3 with decrease in quantum confinement effect, morphology of the nanomaterials and the particle size. The band gap was determined to be 2.3 eV, 2.1 eV and 1.6 eV respectively for BCFO-1, BCFO-2 and BCFO-3 nanomaterials. However there is a gradual decrease in the band gap when the substituent concentration is increased which confirms the red shift in the metastable state of the band gap. In this work the optical data's of the nanomaterials is changed by the addition of Cu^{2+} substituent. From Table 5, it is clearly seen that when the copper is substituted in smaller concentration there is minor red shift is determined. This red shift can be called as pressure induced effects. When the as-synthesized nanomaterial experience this type of pressure on its surface, leads to increase in lattice strain and makes the nanomaterial to be a hard magnet and this optical activity stands as a progressive step for the degradation of the organic pollutants like Methylene blue dye.

Table 4. Pore volume, pore diameter and surface area parameters of BCFO -1, BCFO-2, BCFO-3 nanomaterials

Compound name	Copper concentration (x)	Crystallite size from PXRD (nm)	Pore volume (cc/g)	Pore diameter (nm)
BCFO-1	0	21	0.006	1.594
BCFO-2	0.6	25	0.003	2.156
BCFO-3	1	22	0.010	1.594

Photocatalytic studies:

Photocatalytic degradation studies for the synthesized nanomaterials were carried out in HEBER multi lamp photo reactor. The nanomaterials synthesized clearly showed the absorption in the visible-light region. The band gap around 1.5–4 eV enable them to adsorb visible light to produce electron-hole. This electron-hole pairs tend to recombine and reduce the efficiency to degrade the organic pollutants. The photocatalytic experiment was carried out by taking 100 mg of the catalyst and 100 mL of 25 ppm Methylene blue dye solution. Cu^{2+} capture the photo generated electron from the peroxide, which improves the photocatalytic activity of the

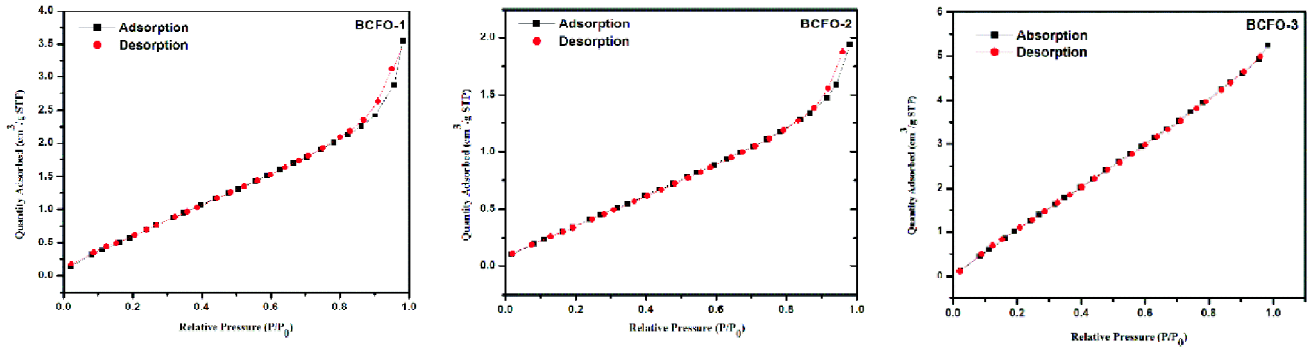

Fig. 5. BET isotherms for BCFO-1, BCFO-2 and BCFO-3 nanomaterials.

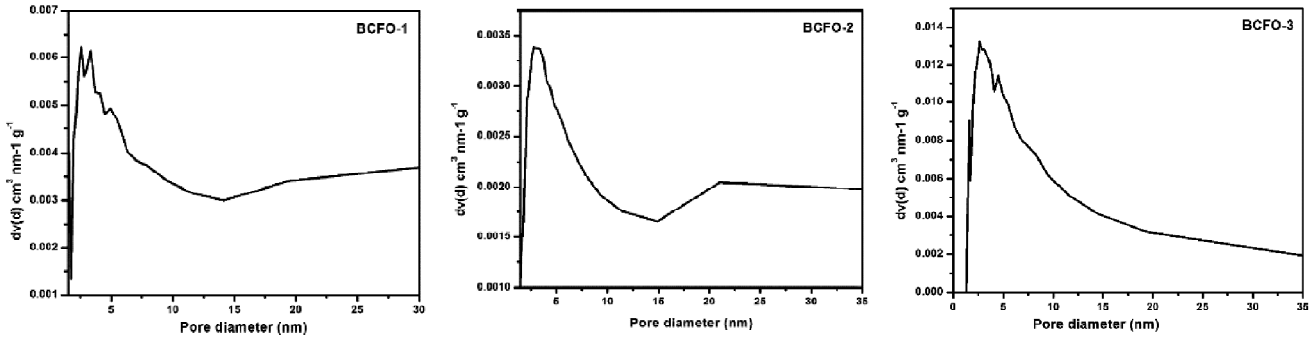

Fig. 5.1. Pore diameter graphs for BCFO-1, BCFO-2 and BCFO-3 nanomaterials.

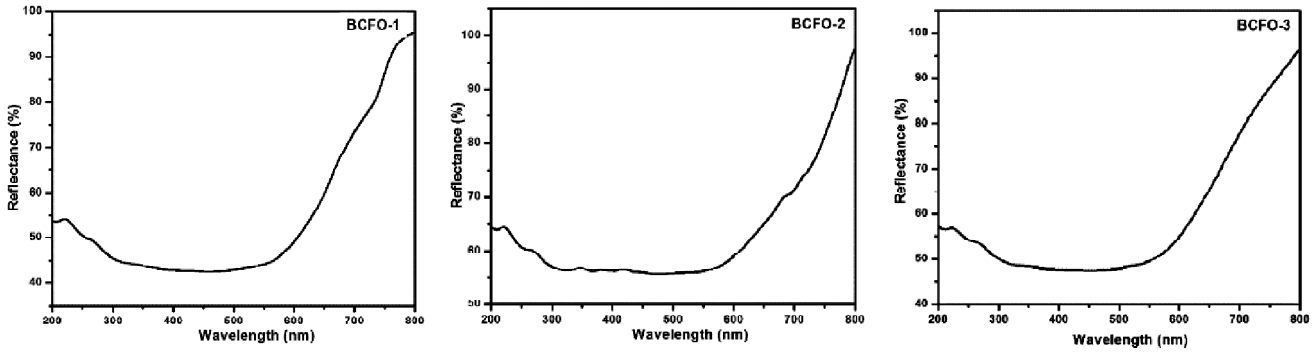

Fig. 6. UV-Visible spectra for BCFO-1, BCFO-2 and BCFO-3 nanomaterials.

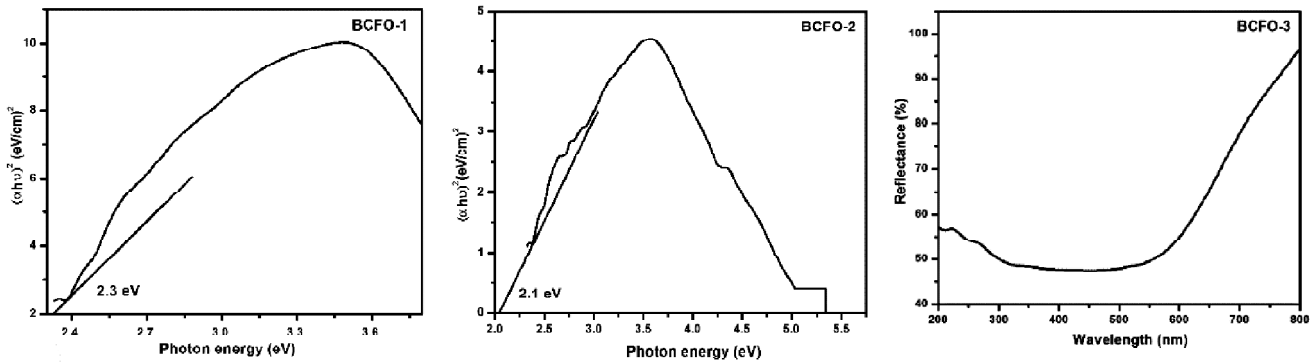

Fig. 6a. Band gap spectra for BCFO-1, BCFO-2 and BCFO-3 nanomaterials.

Table 5

Sl. No.	Bacteria	Standard Streptomycin	BCFO-1 25 mg	BCFO-1 50 mg	BCFO-2 25 mg	BCFO-2 50 mg	BCFO-3 25 mg	BCFO-3 50 mg	BCFO-4 25 mg	BCFO-4 50 mg	BCFO-5 25 mg	BCFO-5 50 mg	BCFO-6 25 mg	BCFO-6 50 mg
1.	*Enterobacter aerogenes*	19 mm	+	11 mm	10 mm	10 mm	10 mm	12 mm	12 mm	+	10 mm	10 mm	12 mm	10 mm
2.	*Staphylococcus aureus*	16 mm	13 mm	+	+	12 mm	ND	13 mm	ND	+	13 mm	+	+	11 mm
3.	*Bacillus subtilis*	20 mm	ND	+	ND	+	+	+	+	+	ND	ND	ND	+
4.	*Escherichia coli*	16 mm	+	+	12 mm	+	+	10 mm	10 mm	+	+	+	+	+
5.	*Micrococcus luteus*	14 mm	10 mm	11 mm	12 mm	13 mm	+	12 mm	11 mm	10 mm	+	+	10 mm	10 mm
				+	+	+	12 mm	10 mm	+	10 mm	11 mm	+	+	10 mm

Note: ND: Not detected. +: Partial inhibition

synthesized nanomaterial. In photocatalytic reaction the initial 30 min were done in the absence of UV irradiation lamp. The concentration of Methylene blue dye degraded exponentially with photocatalytic reaction time and low photocatalytic decolourization was observed, 1%, 12% and 7.9% for BCFO-1, BCFO-2 and BCFO-3 spinel oxides respectively. The photocatalytic studies were done for three hours under UV-lamp irradiation and the samples were taken for every 30 min and measured with UV-Visible spectrophotometer. The intensity of the main absorption band at 665 nm decreases with increase in time. Absorption spectra (Fig. 7) showed 94% degradation for $Ba_{1-x}Cu_xFe_2O_4$ spinel ferrites which are due to Cu^{2+} addition and this increase in Cu^{2+} enhance the good photocatalytic application for the synthesized nanomaterials. Decrease in crystallite size also increases the photoionic efficiency from a higher interfacial charge carrier transfer rate[20,21]. This shows the photodecomposition activity for Methylene blue dye against the synthesized nanocatalysts. The following equation was used to determine the percentage degradation of the nanomaterials.

$$\% \text{ Degradation} = C_o - C_t/C_o$$

where, C_o is the initial concentration and C_t is the concentration of the sample to undergo reaction at time t.

Degradation kinectics:

The adsorption kinetics provides information about the mechanism of adsorption of Methylene blue dye in the presence of synthesized photocatalyst. The photodegradation study followed pseudo-first order kinetics in the presence of UV-lamp and the following equation was used to determine the degradation kinectics of the nanomaterials.

$$\ln (C_o/C) = kC$$

where k is rate constant and C_o is the initial concentration and C is the remaining concentration at time, t for the synthesized photocatalyst. From the above kinectics equation we gets linear plot (Fig. 8) which confirms the pseudo-first order kinetics of Langmuir-Hinshelwood relationship of bimolecular reaction. Where, the Methylene blue dye which is adsorbed on the photocatalyst sites undergoes to form a bimolecular reaction. Fig. 8.1 showed the degradation efficiency for the synthesized nanomaterials.

Antibacterial activity:

The antibacterial activity of the $Ba_{1-x}Cu_xFe_2O_4$ spinel

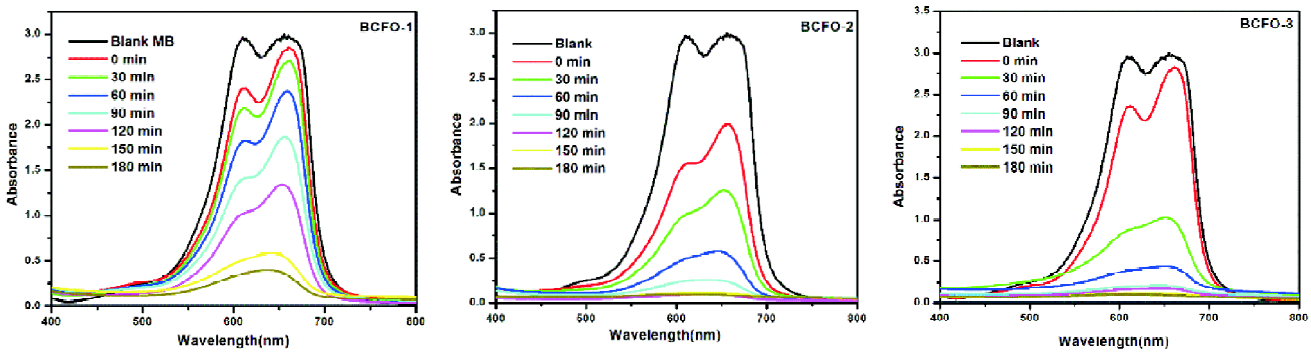

Fig. 7. Absorption spectra for BCFO-1, BCFO-2 and BCFO-3 nanomaterials.

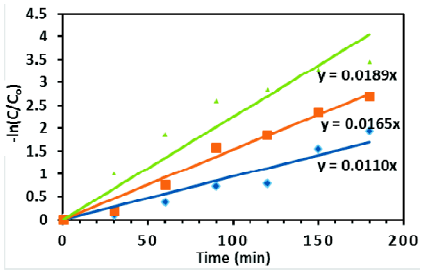

Fig. 8. Pseudo-first order kinetic plot for BCFO-1, BCFO-2 and BCFO-3 nanomaterials.

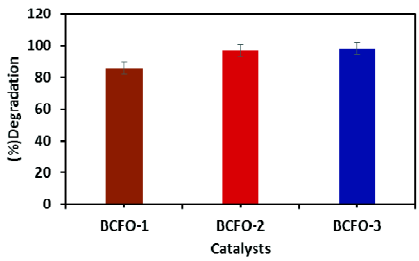

Fig. 8.1. Degradation efficiency of BCFO-1, BCFO-2 and BCFO-3 nanomaterials.

ferrites was studied using Agar well diffusion method by calculating the diameter of the growth inhibition zone. $Ba_{1-x}Cu_xFe_2O_4$ nanomaterials showed maximum antibacterial activity against *Enterobacter aerogenes* (Gram-negative) and *Escherichia coli* (Gram-negative). The absence of bacterial development around the synthesized nanomaterial is an indirect measure of the ability of the nanomaterial to inhibit the growth of the bacteria. Table 6 gives the zone of inhibition for all the five microorganisms[26,27].

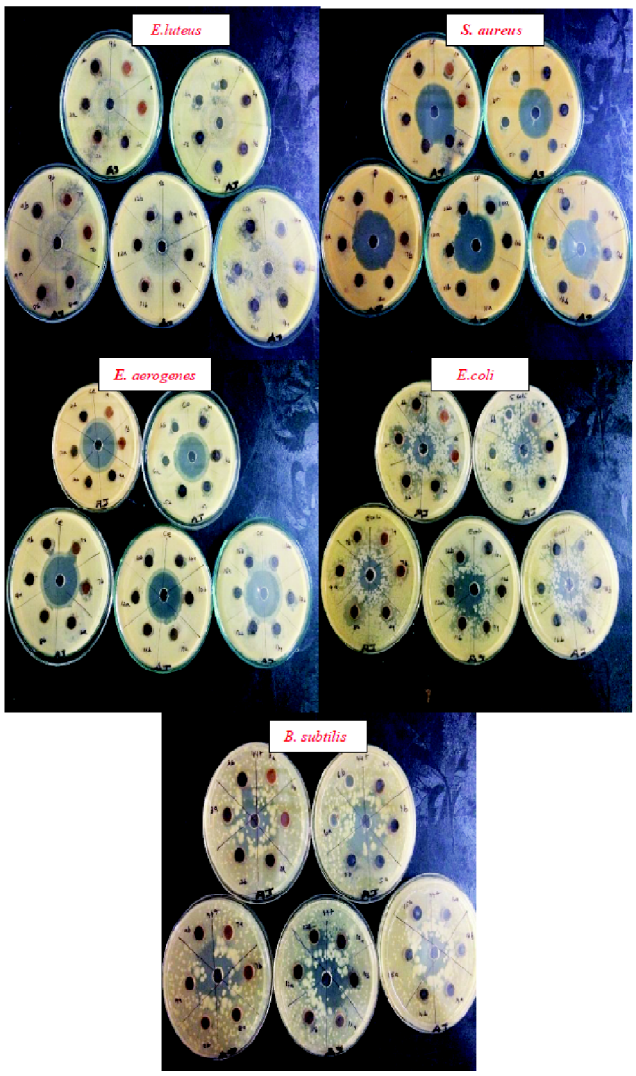

Fig. 9. Antibacterial activity of BCFO nanomaterials.

Conclusions

In this work we have synthesized copper substituted barium ferrite nanomaterials by cost-effective and chemical co-precipitation method. The PXRD diffraction pattern revealed that the synthesized ferrites are nanocrystalline with the crystallite size of about 18–30 nm. The FT-IR spectrum showed characteristic absorption bands at 586 and 421 cm^{-1} corresponding to the stretching vibration modes of tetrahedral and octahedral sites responsible for the spinel ferrite oxides. TEM micrographs showed the distribution of rod shape morphology on the surface. VSM analysis showed the soft and hard ferrite nature of the as-synthesized nanomaterial and the increase in coercivity value due to its magneto crystalline anisotropic effect. To conclude, the present study revealed the role of copper substituted barium ferrite in the degradation of (94% in 180 min) Methylene blue dye under visible light, thus delivering high photon-fenton activity and stability for the as-synthesized nanophotocatalyst.

Acknowledgements

The authors are grateful to the analytical services rendered by DST-FIST Lab, Centre for Research in Science and Technology (CRIST), Stella Maris College (Autonomous), Chennai and we would like to express our sincere thanks to Ms. Jansi Rozario, Department of Bioinformatics, Stella Maris College for her support in doing the antibacterial studies.

References

1. Aylin Gurbuz, Nurhan Onar, Ismail Ozdemir, Abdullah Cahit Karaoglanli and Erdal Celik, *Mater. Tech.,* 2012, **463**, 305.
2. M. M. Rashad, R. M. Mohamed, M. A. Ibrahim, L. F. M. Ismail and E. A. Abdel-Aal, *Ad. Pow. Tech.,* 2012, **233**, 15.
3. S. Vadivelan and N. Victor Jaya, *Int. J. Chem. Tech. Res.,* 2015, **8(12)**, 404.
4. Silvana Da Dalt, Bruna Berti Sousa, Annelise Kopp Alves and Carlos Pérez Bergmann, *Mat. Res*., 2011, **14**, 4.
5. P. H. Borse, C. R. Cho, K. T. Lim, Y. J. Lee, T. E. Hong, J. S. Bae, E. D. Jeong, H. J. Kim and H. G. Kim, *J. Kor. Phy. Soc.*, 2011, **58(6)**, 1672.
6. Jiong Zhoua, HongliangMa, Minjian Zhong, Guoqing Xu, Zhongyue Yue and Zhengming He, *J. Mag. Mag. Mat.,* 2006, **305**, 467.
7. C. Valero-Lunaa, S. A. Palomares-Sanchéza and Facundo Ruíza, *Cat. Today*, 2015, 0920.
8. Kai Huang, Xiansong Liu, Shuangjiu Feng, Jiangying Yu, Xiaofei Niu, Farui Lv and Xing Huang, *Mat. Tech. Adv. Per. Mat.*, 2016.
9. M. K. Mustafa, A. F. Ismai, M. H. D. Othman, Mukhlis, A. Rahman and Alireza Samavati, *Mat. Express*, 2016, **6(6)**.
10. Krishnan Muthukumar, D. Shanthana Lakshmi, Saranya D. Acharya, S. Natarjan, Amitava Mukerje and H. C. Bajaj, *Mat. Chem. Phys.,* **18**, 0254.
11. S. Vadivelan and N. Victor Jaya, *Results in Physics*, 2016, 2211.
12. C. Maria Magdalane, K. Kaviyarasu, J. Judith Vijaya, Busi Siddhardha and B. Jeyaraj, *J. Photochem. Photo. B: Bio.,* 2016, **163**, 77.
13. Sami H. Mahmood and Ibrahim B. Soul, "Tuning the Magnetic Properties of M-type Hexaferrites".
14. R. C. Pullar, *Pro. Mat. Sci.*, 2012, **57**, 1191.
15. M. Saranya and Balavijayalakshmi, *J. Nanosci. Nanotechnol.,* 2014, **2**, 397.
16. H. Moradmard, S. Farjami Shayesteh, P. Tohidi, Z. Abbas and M. Khaleghi, *J. Alloys. Compd.,* 2015, **15**, 0666.
17. Sami H. Mahmood, Ahmad Awadallah, Yazan Maswadeh and Ibrahim B. Soul, *Mat. Sci. Engineering,* 2015, **92**, 012.
18. A. Pasko, F. Mazaleyrat, M. Lo Bue, V. Loyau, V. Basso, M. Küpferling, C. P. Sasso and L. Bessais, *J. Phys.,* 2011, **303**, 012045.
19. S. H. Mahmood, Q. Al-Shiab, I. Bsoul, Y. Maswadeh and A. Awadallah, "Structural and magnetic properties of (Mg, $Co)_2W$ hexaferrites".
20. John D. Rodney, S. Deepapriya, P. Annie Vinosha, S. Krishnan, S. Janet Priscilla, R. Daniel and S. Jerome Das, *Optik*, 2018, **161**, 204.
21. P. Annie Vinosha, Belina Xavier, S. Krishnan and S. Jerome Das, *Materials Research Bulletin,* 2018, **101**, 190.
22. A. Khorsand Zak, W. H. Abd. Majid, M. E. Abrishami and Ramin Yousefi, *Solid State Sci.,* 2011, **13**, 251.
23. Yendrapati Taraka Prabhu, Kalagadda Venkateswara Rao, Vemula Sesha Sai Kumar and Bandla Siva Kumari, *World J. Nano Sci. Engineering,* 2014, **4**, 21.
24. S. Vadivelan and N. Victor Jaya, *Results in Physics*, 2016, 2211.
25. A. Morrish, X. Zhou, Z. Yang and H.-X. Zeng, *Interactions*, 1994, **90**, 365.
26. Sheena Xavier, Harry Cleetus, Nimila, Smitha Thankachan, Rintu Mary Sebastian and E. M. Mohammed, *Res. J. Pharm., Bio. Chem. Sci. RJPBCS*, 2014, **5(5)**, 364.
27. Sami H. Mahmood, Abdelkarim A. Ghanem, Ibrahim B. Soul, Ahmad, Awadallah and Yazan Maswadeh, *Mater. Res. Express*, 2017.